separations

MDPI

Article

Effective Utilization of Sulfur Wastewater by Photocatalytic System Using B/CuO/ZnO

Ikki Tateishi [1,*], Mai Furukawa [2], Hideyuki Katsumata [2] and Satoshi Kaneco [1,2]

[1] Mie Global Environment Center for Education & Research, Tsu City 514-8507, Japan; kaneco@chem.mie-u.ac.jp
[2] Department of Chemistry for Materials, Graduate School of Engineering, Mie University, Tsu City 514-8507, Japan; maif@chem.mie-u.ac.jp (M.F.); hidek@chem.mie-u.ac.jp (H.K.)
* Correspondence: tateishi@gecer.mie-u.ac.jp; Tel.: +81-59-231-9647

Abstract: B-doped zinc oxide/copper oxide composites prepared using a simple method showed high photocatalytic hydrogen production activity in the presence of aqueous sulfide solutions. Co-modification of the CuO composite with B-doping caused an increase in the charge separation efficiency and light absorption capacity. The sacrificial effect was thermodynamically enhanced by manipulating the composition of the sulfide solution. A maximum hydrogen production activity of 224 μmol g^{-1} h^{-1} was achieved under 450 nm light irradiation in a photocatalytic system with optimized B doping, a CuO composite, and a sulfide sacrificial agent concentration.

Keywords: photocatalysis; ZnO; visible light; B-doped; CuO; purification of sulfide effluent

Citation: Tateishi, I.; Furukawa, M.; Katsumata, H.; Kaneco, S. Effective Utilization of Sulfur Wastewater by Photocatalytic System Using B/CuO/ZnO. *Separations* **2024**, *11*, 19. https://doi.org/10.3390/separations11010019

Academic Editors: Gavino Sanna and Qicheng Feng

Received: 17 November 2023
Revised: 20 December 2023
Accepted: 29 December 2023
Published: 5 January 2024

1. Introduction

Sulfur occurs in various chemical forms in nature, such as in the ground and seawater. Industrial anthropogenic activities, such as oil refining, mining, and natural gas processing, result in the discharge of significant amounts of sulfides in wastewater [1,2]. The presence of toxic sulfides in wastewater results in high biological oxygen demand and poses a threat to the biological environment in the water [3]. Thus, if discharged to water bodies without treatment, they can cause serious environmental problems, including damage to aquatic life [4]. In light of this, the treatment of sulfides in wastewater is often attempted using various chemical treatment processes, such as adsorption, coagulation, chemical oxidation, and biological processes, in order to avoid associated environmental problems. However, most chemical technologies require large chemical dosages and consume large amounts of energy, making them either expensive to operate or environmentally unfriendly [5–9]. Photocatalysts are non-toxic and stable and use light as the driving energy to mineralize organic pollutants. Therefore, the photocatalytic approach using sunlight as the light source is sustainable and cost-effective [10–14]. ZnO is a typical semiconductor with a direct band gap that can be utilized as a photocatalyst and has been used for the photocatalytic degradation of several dye pollutants and photocatalytic H_2 production [15–20]. However, their photocatalytic efficiency is limited by their low energy utilization under visible light, small specific surface area for active sites, and susceptibility to photogenerated electron–hole charge pair recombination. Several works were undertaken to improve the photocatalytic activity of ZnO using heterojunction and doping methods to overcome these drawbacks, improve the chemical behavior, and achieve efficiencies suitable for practical applications [21–25].

Doping zinc oxide with non-metallic elements, such as nitrogen, carbon, and boron, enhances the photocatalytic activity by extending the light absorption wavelength and suppressing the recombination of photogenerated electron–hole pairs through the manipulation of the band structure due to the formation of impurity positions [26–28]. Boron has emerged as a very promising nonmetal candidate for integration and diffusion into

the semiconductor lattice in the widely studied dopant arena due to its attractive physicochemical properties, including being lightweight, having high chemical resistance, and characteristic semiconducting properties. Compared with the other nonmetallic ions mentioned earlier, boron has the smallest ionic radius (0.023 nm), allowing for its seamless incorporation into the semiconductor crystal framework. Furthermore, boric acid serves as an environmentally friendly and cost-effective source of boron, is easy to handle, and is already widely used in a variety of industrial processes. In particular, the electron configuration of boron is electron deficient due to the vacancy of one p orbital. As a result, the chemical environment surrounding each boron atom is governed by its electron-deficient nature, which is expected to promote charge separation in photocatalytic reactions. CuO exhibits impressive physical and chemical properties, including adequate redox potential, electrochemical activity, excellent thermal conductivity, and outstanding stability in solution. CuO has also attracted significant attention as a promising alternative to precious metals in the area of photocatalytic hydrogen production due to its excellent photocatalytic performance, abundant availability, cost-effectiveness, easy synthesis, and various structural variations. CuO is composed of Cu 3d and O 2p shells, with conduction band (CB) and valence band (VB) edges, which allows for the effective absorption of visible light across the infrared spectrum. This opens up the possibility of a synergistic combination with wide bandgap semiconductor photocatalysts. Heterojunction photocatalysts have a superior ability to extend the photoresponse range and promote the separation of photogenerated charge carriers compared with single-phase photocatalysts by forming band bends [29,30]. Choi et al. researched a cost-effective and environmentally friendly photocatalytic approach that was responsive to light and was employed to investigate the enhancement of hydrogen production efficiency in ZnO through copper doping via water–methanol solution decomposition. The author synthesized efficient nanocomposites of ZnO doped with varying copper proportions (0.0, 0.01, 0.03, 0.05 mol %) using the sol–gel method and assessed their H_2 evolution. The incorporation of Cu did not alter the hexagonal wurtzite structure of the ZnO nanoparticles. Furthermore, the introduction of Cu into ZnO resulted in a reduction of the energy bandgap from 3.19 eV to 3.00 eV. Notably, the rate of photoinduced electron and hole recombination decreased with increasing Cu doping levels. The ZnO catalyst incorporating Cu exhibited an increase in H_2 production, rising from 7.49 μmol g^{-1} to 41.55 μmol g^{-1}. This enhancement in H_2 production with Cu-doped ZnO nanoparticles is attributed to the decreased recombination rate of electrons and holes during the photocatalytic hydrogen production [31]. Monzoor et al. utilized a conventional hydrothermal method to synthesize ZnO nanoparticles (Cu_xZn_yO) incorporating various levels of Cu (0.1, 0.5, 1.0, and 5.0 mol%). It was ascertained that Cu ions are effectively integrated into the ZnO framework, resulting in a reduction in crystallite size as the Cu ion content increases. The study revealed that the introduction of Cu ions into ZnO leads to an augmentation in photocatalytic activity, which is primarily attributed to the broadening of the light absorption spectrum and a decrease in the recombination rate of photogenerated charge carriers. Significantly, the H_2 production activity of the Cu-doped ZnO catalyst surpasses that of the pure ZnO catalyst. Among the various samples tested, the $Cu_{0.01}$ $Zn_{0.99}$ O catalyst with 1.0 mol% Cu exhibits the highest H_2 production activity. This improved H_2 production activity in the Cu_xZn_yO catalyst can be attributed to the extended lifetime of excited electrons and the reduced recombination rate of electrons and holes during the photocatalytic reaction [32]. Sun et al. successfully synthesized a novel series of $Bi_{1.5}Zn_{1-x}Cu_xTa_{1.5}O_7$ (Cu-α-BZT) photocatalysts with a pyrochlore structure using the solid-state reaction technique. The products underwent characterization to assess their phase structure, morphology, optical properties, energy levels, and specific surface area. The unadulterated α-BZT exhibited substantial photocatalytic activity when subjected to UV irradiation. Furthermore, the incorporation of copper through the doping process improved the photocatalytic performance of α-BZT. The UV-visible spectrum of the Cu-α-BZT sample demonstrated visible light responsiveness, which can be attributed to the transition from the donor level generated by copper impurities to the conduction band of

α-BZT. It is noteworthy that Cu-α-BZT displayed optimal activity when the doping amount (x) was 0.01 as a molar ratio, achieving an impressive 45 μmol h^{-1} g^{-1} of photocatalytic hydrogen evolution [33]. Li et al. presented a straightforward technique for producing hollow-structured Cu/TiO_2 photocatalysts utilizing templates from metal-organic frameworks (MOFs). This approach allows for the adjustment of the photocatalyst's composition, crystalline phase, cocatalyst size, and more by simply modifying the MOF core processing conditions, which include room-temperature etching, simultaneous etching and reduction, and high-temperature calcination, providing remarkable versatility. In comparison with the commonly employed calcination method, simultaneous etching and reduction not only better preserves the octahedral-shaped shell and crystalline phase but also prevents the formation of carbon residues and the agglomeration of cocatalysts. These factors collectively contribute to enhanced photocatalyst efficiency. The octahedral shell photocatalysts created in this manner exhibit distinct performance variations in charge separation and photocatalytic hydrogen production under different configurations, enabling the identification of the most effective photocatalyst design. The optimized Cu/TiO_2 photocatalyst demonstrated a high hydrogen production rate of 62.16 μmol g^{-1} h^{-1} under UV light [34]. Chen et al. employed an in situ growth method to create a novel composite photocatalyst composed of CuS and g-C_3N_4. CuS nanoparticles, with an average diameter of approximately 10 nm, were effectively dispersed on the surface of g-C_3N_4, underscoring the potential of g-C_3N_4 nanosheets as a promising substrate for the in situ growth of nanoscale materials. Within this system, electrons originating from the valence band (VB) of g-C_3N_4 were directly transferred to the CuS cluster, leading to the partial reduction of CuS to Cu_2S. The latter acted as both an electron sink and a cocatalyst, thereby enhancing the separation and mobility of CuS clusters. As a result of this efficient interfacial charge transfer, the CuS/g-C_3N_4 composite demonstrated a significantly improved visible-light-driven photocatalytic hydrogen generation through water splitting when compared with pure g-C_3N_4. The peak photocatalytic activity was observed in the case of a 2 wt% CuS/g-C_3N_4 composite photocatalyst, achieving a hydrogen production rate approximately 13.76 times higher than that of pure g-C_3N_4, which was primarily due to the enhanced interplay of charge carriers [35]. Xing et al. fabricated nanocomposites of 2D $MoSe_2$/TiO_2 using a straightforward hydrothermal method, employing two-dimensional $MoSe_2$ nanosheets and P25 as precursor materials. It was demonstrated that the inclusion of $MoSe_2$ effectively augmented the light absorption capacity of the resulting nanocomposite. Moreover, the $MoSe_2$/TiO_2 heterojunction exhibited minimal electron and hole recombination. Photocatalytic hydrogen evolution assessments revealed that the hydrogen production rate for the sample containing 0.1 wt % $MoSe_2$ was 4.9 μmol h^{-1}, which represented a twofold increase in comparison with pristine TiO_2 [36]. Xing et al. developed a BCN-TiO_2(A+R) nanocomposite with a one-step calcination process, using NTA and BCN as the precursor materials, resulting in a combination of anatase and rutile phases. This composite exhibited a unique heterojunction and phase junction, leading to a close interface and extensive contact area between the two semiconductor components, thereby broadening the range of visible light absorption. Consequently, BCN-TiO_2(A+R), which features a blend of anatase and rutile phases, produces an extended charge carrier lifetime and enhanced photocarrier separation efficiency owing to the synergistic effects of the heterojunction and phase junction, akin to pure TiO_2. In comparison, the electron lifetime was increased by a factor of 11, resulting in remarkable photocatalytic hydrogen production with a rate of 68.5 μmol h^{-1} g^{-1}. This rate surpasses the photocatalytic performance of TiO_2(A+R) and pure BCN by approximately 7.5 and 12.2 times, respectively [37]. Utilizing a one-step hydrothermal method, Tanaka et al. showcased the environmentally friendly and straightforward synthesis of their high-performance TiO_2/GS photocatalyst. This catalyst demonstrates the ability to leverage a sulfide solution as a sacrificial agent, capturing photogenerated holes for the purpose of photocatalytic hydrogen production. Notably, this method allows for the simultaneous reduction of graphene oxide (GO) and the generation of TiO_2. XRD results reveal that the presence of graphene sheets (GS) inhibits crystal growth and facilitates the formation of

the rutile phase. The TiO_2/GS photocatalyst obtained using this process exhibits superior activity compared with P25. This enhancement was attributed to the favorable electronic conductivity of GS and the establishment of a chemical bond between TiO_2 and GS. The researchers anticipated that the photocatalytic activity of TiO_2/GS can be further improved by optimizing parameters such as the initial $TiCl_4$ concentration and hydrothermal conditions [38]. Tanaka et al. synthesized mesoporous ZnS and ZnO nanoplates using the calcination of a solvothermally prepared ZnS(en)0.5 complex (en = ethylenediamine), with ethylenediamine serving as the exclusive solvent. The heating of the $ZnS(en)_{0.5}$ complex resulted in the formation of mesoporous nanoplates with a wurtzite-type ZnS structure, which further oxidized into ZnO platelets. The transformation process from $ZnS(en)_{0.5}$ to ZnS to ZnO appeared to be topotic, indicating structural and pseudomorphic crystallographic relationships between the three solid phases. The photocatalytic performance of the material was assessed for hydrogen production from a Na_2S/Na_2SO_3 aqueous solution and the decomposition of the azo dye Acid Red 14. ZnS calcined at 500 °C exhibited the highest hydrogen production rate using water decomposition under visible light irradiation. In contrast, ZnO demonstrated the highest hydrogen production rate when calcined at 550–600 °C, showcasing its efficacy in the photocatalytic decomposition of the dye under UV irradiation [39]. Y.M. Hunge et al. embarked on the synthesis of a revolutionary binary photocatalyst, namely, the MoS_2/ZnO composite, by employing a sophisticated hydrothermal route. This novel composite was designed to leverage the unique properties of molybdenum disulfide (MoS_2) and zinc oxide (ZnO), combining them synergistically to create a photocatalyst with enhanced visible light absorption capabilities. The integration of MoS_2, which is a lower bandgap semiconductor, with ZnO was found to significantly augment the visible light absorption efficiency of the latter, as revealed by comprehensive optical studies. The MoS_2/ZnO composite thus formed emerged as a highly efficient visible-light-induced photocatalyst, demonstrating exceptional prowess in the decomposition of organic compounds and hydrogen production. The hydrogen production rates were measured at 22, 39, and an impressive 235 μmol g^{-1} h^{-1} for ZnO, MoS_2, and the MoS_2/ZnO composite, respectively. This remarkable enhancement in hydrogen production efficiency in the presence of the MoS_2/ZnO composite underscores its potential as a promising candidate for sustainable energy applications [40].

Our previous work has provided a low-cost, highly active method for hydrogen production using B-doped zinc oxide/zinc sulfide/copper sulfide photocatalysts, combining the nonmetal doping and heterojunction methods, which were prepared using the photocatalytic reaction of B-doped zinc oxide and copper oxide in sulfide solutions. However, optimization under previous visible light irradiation had not been performed. In this study, the optimal conditions for catalyst preparation and the sacrificing agent under visible light irradiation were investigated.

2. Materials and Methods

In this experiment, all chemicals were of analytical purity and used without further purification. The B/CuO/ZnO photocatalyst series was prepared using a one-step thermal method. Various ratios of zinc acetate dihydrate, copper acetate monohydrate, oxalic acid, and boric acid were mechanically well mixed and heat treated in an electric furnace at 500 °C for 3 h under an air atmosphere. ZnO, B/ZnO, and CuO/ZnO were prepared in a similar procedure for comparison.

Powder X-ray diffraction (XRD) patterns were recorded on a Rigaku RINT Ultima-IV diffractometer using a Cu source at a scanning speed of 0.02°/s to identify the chemical structures of the prepared photocatalysts. To determine the binding states of the elements, the bond energy was measured via X-ray photoelectron spectroscopy (XPS) with a PHI Quantera SXM photoelectron spectrometer using an Al Kα radiation source. The measured binding energy was corrected using the C1s peak (284.8 eV) as a reference to eliminate the effects of shifts due to sample charging. The superficial shape of the photocatalyst was observed using a Hitachi S-4000 scanning electron microscope (SEM). The internal structure

was also investigated using a JEOL JEM1011 transmission electron microscope (TEM). To investigate the light absorption characteristics and energy band gap of the photocatalyst, the UV-vis diffuse reflection spectrum (DRS) was recorded using a Shimadzu UV-2450 spectrophotometer using BaSO4 as a reference standard equipped with an integrating sphere attachment. Using a Shimadzu RF-5300PC, the photoluminescence (PL) spectrum of each photocatalyst was detected with an excitation wavelength of 330 nm. To calculate the band gap energy, a classical extrapolation approach was used with the following Equation (1):

$$\alpha h\nu = A(h\nu - Eg)n \quad (1)$$

where hν, α, A, and Eg represent the discrete photon energy, optical absorption coefficient, Planck's constant, and photonic energy band gap, and n = 1/2 for a direct band gap semiconductor.

The photocatalytic hydrogen production experiment was performed in a closed system using a 125 mL Pyrex reactor. An LED lamp (λ = 450 nm, 5.1 mW/cm^2) was used as a side-illuminated visible light source. All photocatalytic hydrogen production experiments were performed in a 40 mL solution kept at 50 °C with a 50 mg catalyst and a Na_2SO_3/Na_2S mixed sacrifice. The reaction system was purged with nitrogen for 30 min before the photocatalytic experiments to remove the dissolved oxygen. The generated H_2 was measured using an online gas chromatograph system (GC) with the thermal conductivity detector (TCD) maintained at 50 °C (Table 1).

Table 1. Experimental conditions.

Photocatalyst	ZnO, B/ZnO, CuO/ZnO, B/CuO/ZnO (50 mg)
Doping amount	B: 0~10 wt% Cu/(Cu + Zn) = 0~20 wt%
Medium	0~0.8 M Na_2S + 0~0.6 M Na_2SO_3 solution (40 mL)
Reactor	Pyrex glass vessel (volume: 125 mL)
Temperature	50 °C
Irradiation time	3 h
Light source	LED lamp (450 nm, ~5.1 mW/cm^2)
Analysis	Gas chromatography (TCD)

3. Results

3.1. Structural Characterization

Figure 1 shows the XRD results of the ZnO, B/ZnO, CuO/ZnO, and B/CuO/ZnO before and after the photocatalytic reaction in a sulfide solution. The hexagonal ZnO-indexed JCPDS card number 361,451 was observed in the sample containing ZnO before the photocatalytic reaction. A weak peak assigned to the CuO-indexed JCPDS card number 450,937 was observed for the feed containing CuO. The photocatalyst after the photocatalytic reaction had diffraction peaks that closely matched the (002), (110), and (112) crystal planes of the hexagonal structure of ZnS shown in JCPDS:05-0492. Also, due to the low CuO content, no CuO peak was detected and no other impurities were observed. The ZnO and CuO/ZnO had peaks corresponding to (100), (002), (101), (103), and (112) planes, respectively. On the other hand, no ZnO peak was observed for B/ZnO and B/ZnO/CuO. The crystallite sizes calculated using the Scherrer equation are shown in Table 2. It can be seen that B/ZnO and B/ZnO/CuO had smaller crystal sizes compared with ZnO and ZnO/CuO. Compared with the XRD spectra before irradiation shown in Figure 1, the decrease in crystallinity of ZnO and CuO was attributed to the sulfidation of the photocatalyst. These results suggest that boron doping caused interactions within the sample structure, reducing the crystal size and promoting surface sulfides.

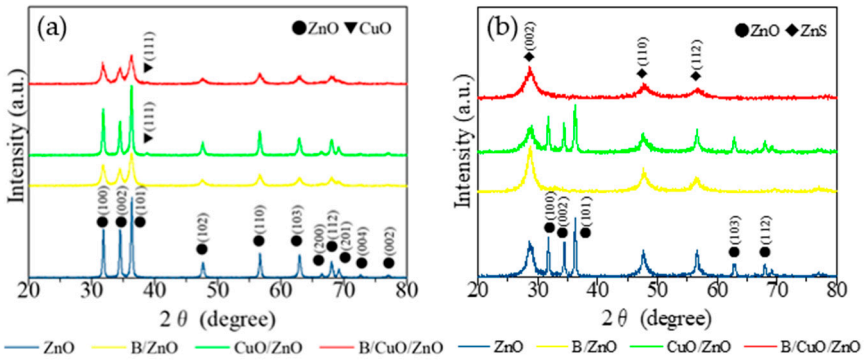

Figure 1. XRD patterns of ZnO, B/ZnO, CuO/ZnO, and B/CuO/ZnO (**a**) before and (**b**) after the photocatalytic reaction in sulfide solution.

Table 2. Crystal size of ZnO, B/ZnO, CuO/ZnO, and B/CuO/ZnO before and after photocatalytic reaction in sulfide solution.

Catalyst	2θ (deg)	Crystal Size (nm)
ZnO	36.321	28.3
B/ZnO	36.149	12.6
CuO/ZnO	36.248	26.4
B/CuO/ZnO	36.26	9.77
ZnO after	36.208	31.7
BZnO after	28.53	6.80
CuO/ZnO after	36.246	21.4
B/CuO/ZnO after	28.92	3.42

To determine the chemical state of each element of the B/CuO/ZnO composite, the sample surface was investigated using XPS and is shown in Figure 2. For comparison, we present the XPS results of the photocatalyst before the photocatalytic reaction in the sulfide solution (Figure S1). The obtained spectrum showed a peak at the binding energy of 1020.4 eV associated with Zn 2p. The positions of the peaks at 161.6 eV and 162.1 eV of S 2p belonged to S 2p3/2 and S 2p1/2, representing ZnS, Cu_2S, and CuS. The Cu 2p XPS spectrum showed a prominent peak at 932.8 eV corresponding to 2p3/2. In the XPS spectrum results showing B 1s, no obvious peak was observed due to the small amount of B doping. The O 1s spectrum showed a peak at 531.0 eV attributed to ZnO and CuO. On the other hand, all the constituent elements were confirmed in the photocatalyst before the photocatalytic reaction in the sulfide solution. The decrease in the B and O peaks after the photocatalytic reaction in the sulfide solution compared with before was due to the sulfidation of the photocatalyst.

3.2. Morphological Analysis

The SEM images of the prepared photocatalysts in sulfide solution after light irradiation are shown in Figure 3. From the SEM images, the prepared photocatalysts were observed to be rectangular secondary particles composed of nano-sized primary particles; the particle shapes of ZnO and CuO/ZnO were larger than those of B/ZnO and B/CuO/ZnO. These results indicate that CuO loading did not change the crystal structure of the ZnO. B doping also induced a decrease in particle size.

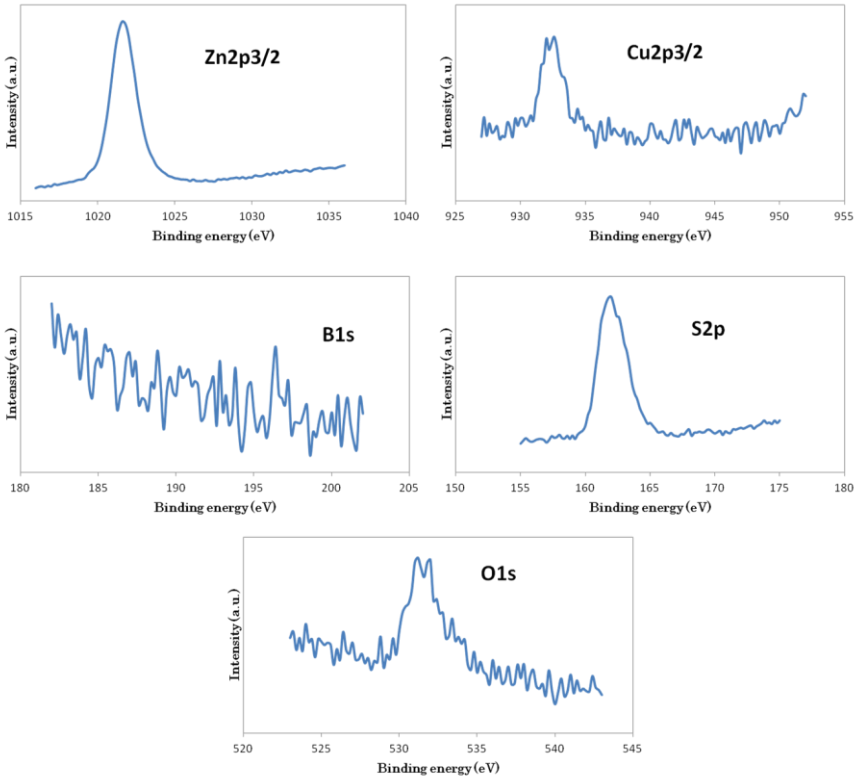

Figure 2. XPS spectra survey of B/CuO/ZnO photocatalyst after photocatalytic reaction in sulfide solution.

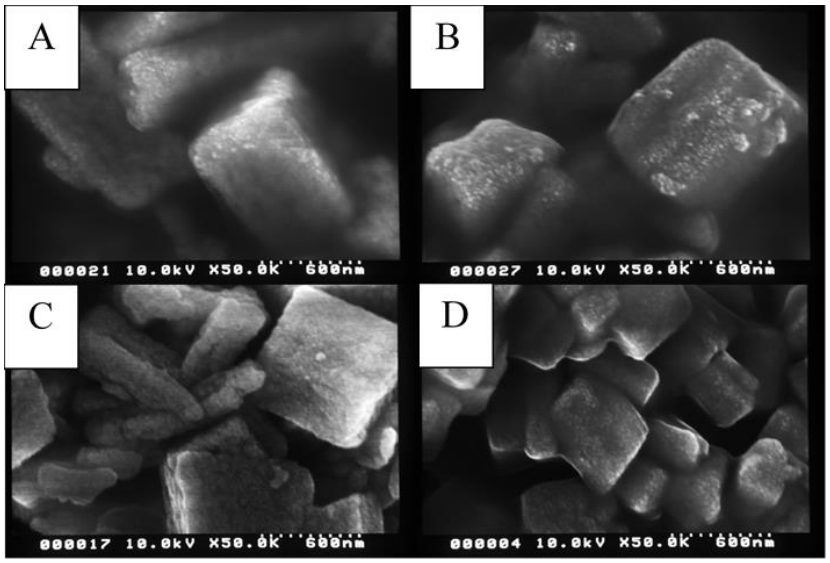

Figure 3. SEM images of (**A**) ZnO, (**B**) B/ZnO, (**C**) CuO/ZnO, and (**D**) B/CuO/ZnO after photocatalytic reaction in sulfide solution.

3.3. Optical Analysis

DRS measurements of each prepared modified photocatalyst are shown in Figure 4. No red shift in the absorption edge was observed with boron doping alone. On the other hand, copper oxide on the catalyst showed absorption at visible wavelengths from 450 nm onward, and the simultaneous loading of boron and copper oxide increased the amount of absorption. The B/CuO/ZnO photocatalyst with the largest increase in absorption showed absorption up to around 500 nm. Photoluminescence measurements of the prepared photocatalysts revealed fluorescence emission. The intensity of the fluorescence emission has generally been considered to be related to exciton transitions and recombination

from the conduction band level to the valence band. The magnitude of the peaks in the fluorescence spectrum decreased in the order ZnO > B/ZnO > ZnO/CuO > B/CuO/ZnO (Figure 5). These results suggest that boron and copper oxide modifications to ZnO decreased the recombination rate of hole–electron pairs and promoted charge separation. From the DRS measurements and Equation (1), the band gap energies of ZnO, B/ZnO, CuO/ZnO, and B/CuO/ZnO were calculated to be 3.27, 3.54, 3.22, and 2.90 eV, respectively.

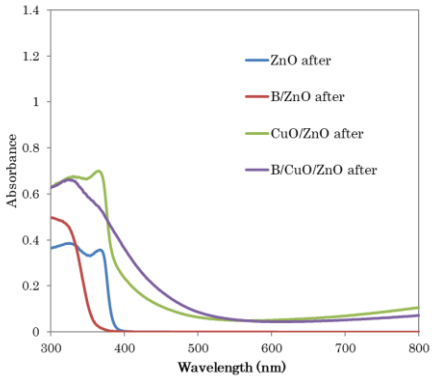

Figure 4. UV-visible spectra of ZnO, B/ZnO, CuO/ZnO, and B/CuO/ZnO after photocatalytic reaction in sulfide solution.

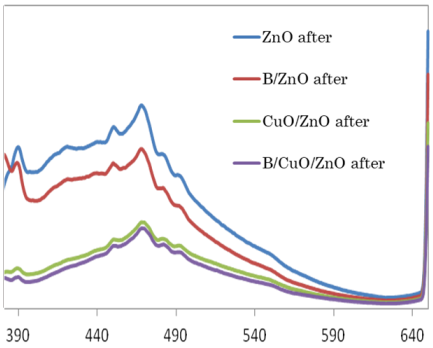

Figure 5. Photoluminescence spectra for ZnO, B/ZnO, CuO/ZnO, and B/CuO/ZnO after photocatalytic reaction in sulfide solution. Excitation: 330 nm.

3.4. Photocatalytic Activity

The experimental conditions were optimized to achieve highly efficient hydrogen production via water splitting using the B/CuO/ZnO photocatalyst system under visible light irradiation. In order to optimize the loading of CuO, the photocatalytic activities of B/CuO/ZnO prepared at the ratios of Cu/(Cu + Zn) (%) = 0, 1, 3, 5, 8, 10, and 20 were compared (Figure 6). A maximum photocatalytic hydrogen production of 490 μmol g^{-1} was achieved when Cu/(Cu + Zn) (%) = 5. The decrease in photocatalytic activity due to the overloading of copper is thought to be due to the light-shielding effect of the copper compound covering the surface of the photocatalyst.

The appropriate amount of boron doping was also investigated (Figure 7). Comparisons of 0, 0.5, 1, 2, 3, 5, and 10 wt% boron doping on the photocatalytic activities showed that 1 wt% was the most effective.

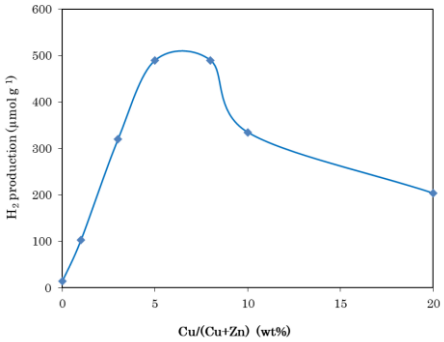

Figure 6. Effect of CuO amount on the photocatalytic hydrogen production with B/CuO/ZnO (B: 2 wt%; Cu/(Cu + Zn) (%) = 0, 1, 3, 5, 8, 10, and 20; and 0.5 M Na_2S + 0.4 M Na_2SO_3 was used as sacrificial agent).

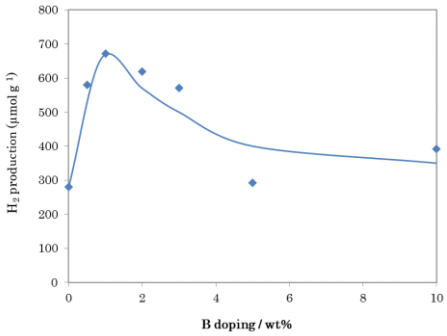

Figure 7. Effect of B doping amount on the photocatalytic hydrogen production with B/CuO/ZnO (B: 0~10 wt%, Cu/(Cu + Zn) = 5 wt%, and 0.5 M Na_2S + 0.4 M Na_2SO_3 was used as sacrificial agent).

The concentrations of aqueous sulfide solutions, which were the solvents used in photocatalytic hydrogen production, were studied in the range of 0 to 0.8 M for Na_2S and 0 to 0.6 M for Na_2SO_3, and the results are shown in Figures 8 and 9. These results suggest that the optimal ratio of Na_2S and Na_2SO_3 as sacrificial agents for photocatalytic reactions thermodynamically promoted the chemical reactions expressed by Equations (6)–(9).

To investigate the stability of the photocatalytic activity exhibited by the prepared photocatalyst, the amount of hydrogen production was measured after 30 h of continuous LED light irradiation. The measurement results show that the photocatalytic activity was hardly deactivated in 30 h (Figure 10).

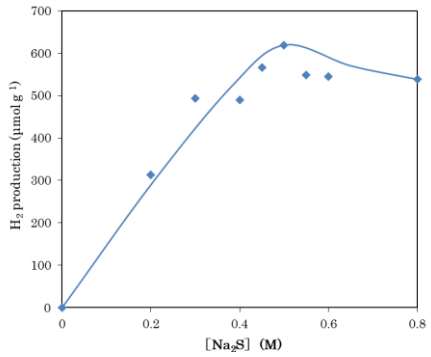

Figure 8. Effect of Na_2S concentration on the photocatalytic hydrogen production with B/CuO/ZnO (B: 2 wt%, Cu/(Cu + Zn) (%) = 5 wt%, and 0~0.8 M Na_2S + 0.4 M Na_2SO_3 was used as sacrificial agent).

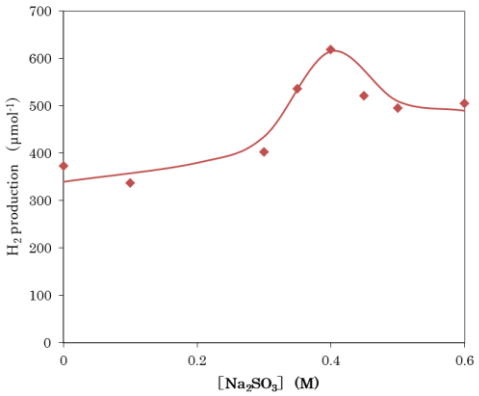

Figure 9. Effect of Na_2SO_3 concentration on the photocatalytic hydrogen production with B/CuO/ZnO (B: 2 wt%, Cu/(Cu + Zn) (%) = 5 wt%, and 0.5 M Na_2S + 0~0.6 M Na_2SO_3 was used as sacrificial agent).

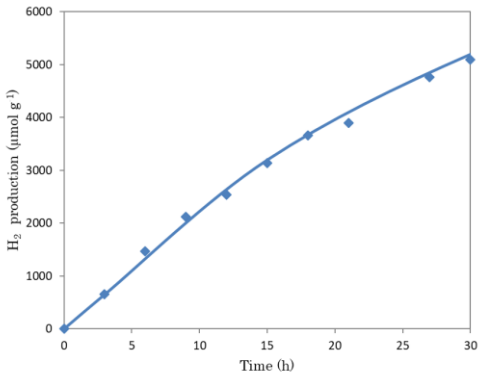

Figure 10. Effect of irradiation time on the photocatalytic hydrogen production with B/CuO/ZnO.

3.5. Proposed Hydrogenation Mechanism

The possible reaction mechanism in this experiment is shown in Figure 11. When the B/CuO/ZnO photocatalyst is added to an aqueous sulfide solution, the surface is sulfurized, resulting in ZnS and CuS. The 450 nm light used in this experiment cannot excite ZnO (3.3 eV) or ZnS (3.6 eV) because of their wide band gaps, but it can excite the energy gap between the conduction band of CuS and the valence band of ZnO (2.2 eV). Therefore, upon irradiation with 450 nm light, electrons in the valence band of ZnO are excited to the conduction band of CuS, producing photoexcited electrons and holes. The generated holes efficiently oxidize sulfide ions and sulfurous acid ions to produce protons, while some of the holes move into the valence band of ZnS. Photoexcited electrons also produce hydrogen according to the following two pathways. In the first reaction pathway, some of the electrons excited in CuS are consumed by Formula (2) to produce Cu_2S, which reduces H^+ to produce H_2 according to Formula (3). In the other reaction pathway, the 450 nm light excites electrons in the valence band of Cu_2S to the conduction band, producing photoexcited electrons and holes. The photoexcited electrons in the conduction band reduce H+ to produce H_2. The holes in the valence band recombine with the photoexcited electrons in the conduction band of CuS and are consumed. The boron loaded in this experiment may have inhibited crystal growth and reduced the crystal size, or it may have created impurity levels in the upper valence band of ZnO, enhancing the charge separation. The purification of sulfide wastewater and reaction equations for aqueous sulfide solutions are shown in (4)–(9). When a semiconductor photocatalyst is irradiated with light, electrons in the valence band are excited to the conduction band, forming hole–electron pairs (Equation (4)). SO_3^{2-} and S^{2-} consume holes and promote the reduction reaction (Equations (6) and (7)) and hydrogen evolution, whereas S_2^{2-}, which is produced by the oxidation of S^{2-}, acts as an optical filter and prevents light absorption (Equation (5)). SO_3^{2-} reacts with S_2^{2-} to

produce $S_2O_3^{2-}$ (Equations (8) and (9)), which does not compete with light absorption, and thus, the coexistence of SO_3^{2-} and S^{2-} is important.

$$2CuS + 2e^- \rightarrow Cu_2S + S^{2-} \quad (2)$$

$$Cu_2S + 2H^+ + S^{2-} \rightarrow 2CuS + H_2 \quad (3)$$

$$\text{Photocatalyst} + h\nu \rightarrow e^-_{CB} + h^+_{VB} \quad (4)$$

$$2H_2O + 2e^-_{CB} \rightarrow H_2 + 2OH^- \quad (5)$$

$$SO_3^{2-} + H_2O + 2h_{VB}^+ \rightarrow SO_4^{2-} + 2H^+ \quad (6)$$

$$2S^{2-} + 2h_{VB}+ \rightarrow S_2^{2-} \quad (7)$$

$$S_2^{2-} + SO_3^{2-} \rightarrow S_2O_3^{2-} + S^{2-} \quad (8)$$

$$SO_3^{2-} + S^{2-} + 2h_{VB}^+ \rightarrow S_2O_3^{2-} \quad (9)$$

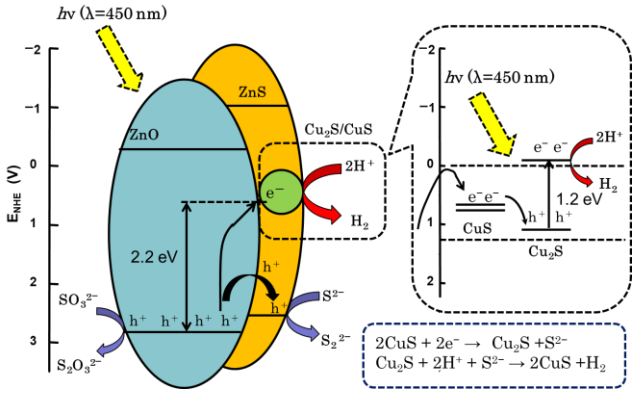

Figure 11. H_2 production mechanism.

Table 3 illustrates the comparison between the outcomes of our research and previously studied achievements in photocatalytic hydrogen generation. The findings from our study were either similar to or outperformed the reported results in the context of photocatalytic hydrogen production.

Table 3. Comparison of photocatalytic hydrogen productions.

Photocatalyst	Medium	Light Source	H_2 Generation (μmol h^{-1} g^{-1})	Ref.
Cu/ZnO	Methanol	UV light	6.9	[31]
Cu/ZnO	Methanol	365 nm	5.84	[32]
$Bi_{1.5}Zn_{0.99}Cu_{0.01}Ta_{1.5}O_7$	$Na_2S + Na_2SO_3$	Xe lamp 300 W	45	[33]
Cu/TiO_2	Methanol	Xe lamp 300 W	62	[34]
CuS/g-C_3N_4	Triethanolamine	Xe lamp 300 W	17.2	[35]
$MoSe_2/TiO_2$	Methanol	Xe lamp 300 W	4.9	[36]
BCN/TiO_2	Triethanolamine	Xe lamp 300 W	68.5	[37]
TiO_2/graphene	$Na_2S + Na_2SO_3$	UV light	108	[38]
ZnS:C	$Na_2S + Na_2SO_3$	Hg lamp 500 W	90	[39]
MoS_2/ZnO	$Na_2S + Na_2SO_3$	Xe lamp 300 W	235	[40]
B/CuO/ZnO	$Na_2S + Na_2SO_3$	LED (450 nm)	224	This work

4. Conclusions

B/CuO/ZnO photocatalysts were prepared using a mechanochemical method, and hydrogen production experiments were performed using 450 nm light in a sulfide solution. The catalytic activity was responsive to visible light by supporting CuO on ZnO. Boron doping promoted the sulfidation of the sample by reducing the crystallite size of ZnO and decreasing the recombination rate of electron–hole pairs. The synergistic effect of these two mechanisms dramatically improved the photocatalytic activity. Also, when the concentration of sulfide solution was Na_2S:Na_2SO_3 = 0.4 M:0.5 M, the maximum photocatalytic hydrogen production activity of 224 μmol g^{-1} h^{-1} was achieved. The results of this study provide certain insights into the effective utilization of sulfide wastewater.

Supplementary Materials: The following supporting information can be downloaded from https://www.mdpi.com/article/10.3390/separations11010019/s1—Figure S1. XPS spectra survey of B/CuO/ZnO photocatalyst before photocatalytc reaction in sulfide solution.

Author Contributions: All authors contributed to this work. Specifically, I.T.: conceptualization, methodology, project administration, writing—original draft preparation, investigation, and data curation. M.F.: writing—reviewing and editing, data curation, and investigation. H.K.: writing—reviewing and editing and resources. S.K.: writing—reviewing and editing and resources. All authors have read and agreed to the published version of the manuscript.

Funding: The authors are grateful to the graduate school department of Mie University for the financial and technical support of this work.

Data Availability Statement: All related data are included in the present paper or available upon request.

Conflicts of Interest: The authors declare no conflicts of interest.

References

1. Henshaw, P.; Medlar, D.; McEwen, J. Selection of a support medium for a fixed-film green sulphur bacteria reactor. *Water Res.* **1999**, *33*, 3107–3110. [CrossRef]
2. Poulton, S.W.; Krom, M.D.; Rijn, J.V.; Raiswell, R. The use of hydrous ion (III) oxides for the removal of hydrogen sulphide in aqueous systems. *Water Res.* **2002**, *36*, 825–834. [CrossRef] [PubMed]
3. Tang, K.; Baskaran, V.; Nemati, M. Bacteria of the sulphur cycle: An overview of microbiology, biokinetics and their role in petroleum and mining industries. *Biochem. Eng. J.* **2009**, *44*, 73–94. [CrossRef]
4. Altas, L.; Buyukgungor, H. Sulphide removal in petroleum wastewater by chemical precipitation. *J. Hazard. Mater.* **2008**, *153*, 462–469. [CrossRef]
5. Syed, M.; Soreanu, G.; Falletta, P.; Béland, M. Removal of hydrogen sulfide from gas streams using biological processes—A review. *Can. Biosyst. Eng.* **2006**, *48*, 2.
6. Klok, J.B.; de Graaff, M.; van den Bosch, P.L.F.; Boelee, N.C.; Keesman, K.J.; Janssen, A.J. A physiologically based kinetic model for bacterial sulfide oxidation. *Water Res.* **2013**, *47*, 483–492. [CrossRef]
7. El-Naas, M.H.; Al-Zuhair, S.; Lobaney, A.A.; Mahlouf, S. Assessment of electrocoagulation for the treatment of petroleum refinery wastewater. *J. Environ. Manag.* **2009**, *91*, 180–185. [CrossRef]
8. Abdelwahab, O.; Amin, N.K.; Ashtoukhy, E.E. Electrochemical removal of phenol from oil refinery wastewater. *J. Hazard. Mater.* **2009**, *163*, 711–716. [CrossRef]
9. Senthil Kumar, P.; Selvakumar, M.; Ganesh Babu, S.; Induja, S.; Karuthapandian, S. CuO/ZnO nanorods: An affordable efficient p-n heterojunction and morphology dependent photocatalytic activity against organic contaminants. *J. Alloys Compd.* **2017**, *701*, 562–573. [CrossRef]
10. Kang, W.; Jimeng, X.; Xitao, W. The effects of ZnO morphology on photocatalytic efficiency of ZnO/RGO nanocomposites. *Appl. Surf. Sci.* **2016**, *360*, 270–275. [CrossRef]
11. Yu, W.; Zhang, J.; Peng, T. New insight into the enhanced photocatalytic activity of N-, C- and S-doped ZnO photocatalysts. *Appl. Catal. B Environ.* **2016**, *181*, 220–227. [CrossRef]
12. Kuriakose, S.; Satpati, B.; Mohapatra, S. Enhanced photocatalytic activity of Co doped ZnO nanodisks and nanorods prepared by a facile wet chemical method. *Phys. Chem.* **2014**, *16*, 12741–12749. [CrossRef] [PubMed]
13. Hui, A.; Ma, J.; Liu, J.; Bao, Y.; Zhang, J. Morphological evolution of Fe doped sea urchin-shaped ZnO nanoparticles with enhanced photocatalytic activity. *J. Alloys Compd.* **2017**, *696*, 639–647. [CrossRef]
14. Sharma, S.; Mehta, S.K.; Kansal, S.K. N doped ZnO/C-dots nanoflowers as visible light driven photocatalyst for the degradation of malachite green dye in aqueous phase. *J. Alloys Compd.* **2017**, *699*, 323–333. [CrossRef]
15. Ullah, R.; Dutta, J. Photocatalytic degradation of organic dyes with manganese-doped ZnO nanoparticles. *J. Hazard. Mater.* **2008**, *156*, 194–200. [CrossRef] [PubMed]

16. Liu, S.; Wang, X.T.; Zhao, W.X.; Wang, K.; Sang, H.X.; He, Z. Synthesis, characterization and enhanced photocatalytic performance of Ag_2S-coupled ZnO/ZnS core/shell nanorods. *J. Alloys Compd.* **2013**, *568*, 84–91. [CrossRef]
17. Zhang, H.; Lv, X.J.; Li, Y.M.; Wang, Y.; Li, J.H. P25-graphene composite as a high performance photocatalyst. *ACS Nano* **2010**, *4*, 380–384. [CrossRef]
18. Jia, T.K.; Wang, W.M.; Long, F.; Fu, Z.Y.; Wang, H.; Zhang, Q.J. Fabrication, characterization and photocatalytic activity of La-doped ZnO nanowires. *J. Alloys Comp.* **2009**, *484*, 410–415. [CrossRef]
19. Tuzemen, E.S.; Kara, K.; Elagoz, S.; Takci, D.K.; Altuntas, I.; Esen, R. Structural and electrical properties of nitrogen-doped ZnO thin films. *Appl. Surf. Sci.* **2014**, *318*, 157–163. [CrossRef]
20. Zhou, D.Z.; Li, B.; Wang, H.L.; Salik, M.; Wu, H.H.; Hu, Z.F.; Gao, S.; Peng, Y.; Yi, L.; Zhang, X.; et al. Fabrication and electrical characterization of Li–N dual doped ZnO thin film transistor. *Appl. Surf. Sci.* **2014**, *305*, 474–476. [CrossRef]
21. Haibo, O.; Feng, H.J.; Cuiyan, L.; Liyun, C.; Jie, F. Synthesis of carbon doped ZnO with a porous structure and its solar-light photocatalytic properties. *Mater. Lett.* **2013**, *111*, 217–220. [CrossRef]
22. Wang, F.; Liang, L.; Shi, L.; Liu, M.; Sun, J. CO_2-assisted synthesis of mesoporous carbon/C-doped ZnO composites for enhanced photocatalytic performance under visible light. *Dalton Trans.* **2014**, *43*, 16441–16449. [CrossRef] [PubMed]
23. Dindar, B.; Guler, A.C. Comparison of facile synthesized N doped, B doped and undoped ZnO for the photocatalytic removal of Rhodamine B. *Environ. Nanotechnol. Monit. Manag.* **2018**, *10*, 457–466. [CrossRef]
24. Gomathisankar, P.; Hachisuka, K.; Katsumata, H.; Suzuki, T.; Funasaka, K.; Kaneco, S. Photocatalytic Hydrogen Production from Aqueous Na_2S + Na_2SO_3 Solution with B-Doped ZnO. *ACS Sustain. Chem. Eng.* **2013**, *1*, 982–988. [CrossRef]
25. Gomathisankar, P.; Hachisuka, K.; Katsumata, H.; Suzuki, T.; Funasaka, K.; Kaneco, S. Photocatalytic hydrogen production from aqueous Na_2SO_3 + Na_2S solution with B/CuO/ZnO under visible light irradiation. *RSC Adv.* **2013**, *3*, 20429–20436. [CrossRef]
26. Malwal, D.; Gopinath, P. CuO-ZnO nanosheets with p–n heterojunction for enhanced visible light mediated photocatalytic activity. *Chemistry* **2017**, *2*, 4866–4873. [CrossRef]
27. Samad, A.; Furukawa, M.; Katsumata, H.; Suzuki, T.; Kaneco, S. Photocatalytic oxidation and simultaneous removal of arsenite with CuO/ZnO photocatalyst. *J. Photochem. Photobiol. A Chem.* **2016**, *325*, 97–103. [CrossRef]
28. Chang, Y.-C. Complex ZnO/ZnS nanocable and nanotube arrays with high performance photocatalytic activity. *J. Alloys Compd.* **2016**, *664*, 538–546. [CrossRef]
29. Kadam, S.R.; Mate, V.R.; Panmand, R.P.; Nikam, L.K.; Kulkarni, M.V.; Sonawane, R.S.; Kale, B.B. A green process for efficient lignin (biomass) degradation and hydrogen production via water splitting using nanostructured C, N, S-doped ZnO under solar light. *RSC Adv.* **2014**, *4*, 60626–60635. [CrossRef]
30. Chen, L.-C.; Tu, Y.-J.; Wang, Y.-S.; Kan, R.-S.; Huang, C.-M. Characterization and photoreactivity of N-, S-, and C-doped ZnO under UV and visible light illumination. *J. Photochem. Photobiol. A* **2008**, *199*, 170–178. [CrossRef]
31. Manzoor, M.F.; Ahmed, E.; Ahmad, M.; Ahmad, I.; Rana, A.M.; Ali, A.; Ghouri, M.I.; Manzoor, M.S.; Aziz, M.T. Enhanced Photocatalytic Activity of Hydrogen Evolution through Cu Incorporated ZnO Nano Composites. *Mater. Sci. Semicond. Process* **2020**, *120*, 105278. [CrossRef]
32. Choi, S.; Do, J.Y.; Lee, J.H.; Ra, C.S.; Kim, S.K.; Kang, M. Optical Properties of Cu-Incorporated ZnO (Cu_xZn_yO) Nanoparticles and Their Photocatalytic Hydrogen Production Performances. *Mater. Chem. Phys.* **2018**, *205*, 206–209. [CrossRef]
33. Sun, J.; Chen, G.; Pei, J.; Jin, R.; Li, Y. A novel $Bi_{1.5}Zn_{1-x}Cu_xTa_{1.5}O_7$ photocatalyst: Water splitting properties under visible light and its electronic structures. *Int. J. Hydrogen Energy* **2012**, *37*, 16960–16966. [CrossRef]
34. Li, R.; Wu, S.; Wan, X.; Xu, H.; Xiong, Y. Cu/TiO_2 octahedral-shell photocatalysts derived from metal–organic framework@semiconductor hybrid structures. *Inorg. Chem. Front.* **2016**, *3*, 104. [CrossRef]
35. Chen, T.; Song, C.; Fan, M.; Hong, Y.; Hu, B.; Yu, L.; Shi, W. In-situ fabrication of CuS/g-C_3N_4 nanocomposites with enhanced photocatalytic H2-production activity via photoinduced interfacial charge transfer. *Int. J. Hydrogen Energy* **2017**, *42*, 12210. [CrossRef]
36. Wu, L.; Shi, S.; Li, Q.; Zhang, X.; Cui, X. TiO_2 nanoparticles modified with 2D $MoSe_2$ for enhanced photocatalytic activity on hydrogen evolution. *Int. J. Hydrogen Energy* **2019**, *44*, 720–728. [CrossRef]
37. Xing, X.; Zhu, H.; Zhang, M.; Xiao, L.; Li, Q.; Yang, J. Effect of heterojunctions and phase-junctions on visible-light photocatalytic hydrogen evolution in BCN-TiO_2 photocatalysts. *Chem. Phys. Lett.* **2019**, *727*, 11–18. [CrossRef]
38. Zhang, X.; Sun, Y.; Cui, X.; Jiang, Z. A green and facile synthesis of TiO_2/graphene nanocomposites and their photocatalytic activity for hydrogen evolution. *Int. J. Hydrogen Energy* **2011**, *37*, 811–815. [CrossRef]
39. Jang, J.S.; Yu, C.J.; Choi, S.H.; Ji, S.M.; Kim, E.S.; Lee, J.S. Topotactic synthesis of mesoporous ZnS and ZnO nanoplates and their photocatalytic activity. *J. Catal.* **2008**, *254*, 144–155. [CrossRef]
40. Yadav, A.A.; Kang, S.-W.; Lim, S.J.; Kim, H. Visible light activated MoS_2/ZnO composites for photocatalytic degradation of ciprofloxacin antibiotic and hydrogen production. *J. Photochem. Photobiol. A* **2023**, *434*, 114250.